

High-Efficiency and Low-Noise Detectors for the Upgraded CLASS 90 GHz Focal Plane

CAROLINA NÚÑEZ,¹ JOHN W. APPEL,¹ RAHUL DATTA,^{1,2} CHARLES L. BENNETT,¹ MICHAEL K. BREWER,¹ SARAH MARIE BRUNO,¹ RICARDO BUSTOS,³ DAVID T. CHUSS,⁴ NICK COSTEN,⁵ JULLIANNA DENES COUTO,⁶ SUMIT DAHAL,⁵ KEVIN L. DENIS,⁵ JOSEPH R. EIMER,¹ THOMAS ESSINGER-HILEMAN,⁵ JEFFREY IULIANO,^{7,1} YUNYANG LI,¹ TOBIAS A. MARRIAGE,¹ JENNETTE MATEO,⁵ MATTHEW A. PETROFF,⁸ RUI SHI,¹ KARWAN ROSTEM,⁵ DENIZ A. N. VALLE,⁶ DUNCAN WATTS,⁹ EDWARD J. WOLLACK,⁵ AND LINGZHEN ZENG⁸

¹The William H. Miller III Department of Physics and Astronomy, Johns Hopkins University, Baltimore, MD 21218, USA

²Department of Astronomy and Astrophysics, University of Chicago, Chicago, IL 60637, USA

³Departamento de Ingeniería Eléctrica, Universidad Católica de la Santísima Concepción, Alonso de Ribera 2850, Concepción, Chile

⁴Department of Physics, Villanova University, Villanova, PA 19085, USA

⁵NASA Goddard Space Flight Center, Greenbelt, MD 20771, USA

⁶Radiosky, San Pedro de Atacama, Chile

⁷Department of Physics and Astronomy, University of Pennsylvania, 209 South 33rd Street, Philadelphia, PA 19104, USA

⁸Center for Astrophysics, Harvard & Smithsonian, Cambridge, MA 02138, USA

⁹Institute of Theoretical Astrophysics, University of Oslo, Oslo, Norway

Submitted to ApJS

ABSTRACT

We present the in-lab and on-sky performance for the upgraded 90 GHz focal plane of the Cosmology Large Angular Scale Surveyor (CLASS), which had four of its seven detector wafers updated during the austral winter of 2022. The update aimed to improve the transition-edge-sensor (TES) stability and bias range and to realize the high optical efficiency of the sensor design. Modifications included revised circuit terminations, electrical contact between the TES superconductor and the normal metal providing the bulk of the bolometer heat capacity, and additional filtering on the TES bias lines. The upgrade was successful: 94% of detectors are stable down to 15% of the normal resistance, providing a wide overlapping range of bias voltages for all TESs on a wafer. The median telescope efficiency improved from $0.42^{+0.15}_{-0.22}$ to $0.60^{+0.10}_{-0.32}$ (68% quantiles). For the four upgraded wafers alone, median telescope efficiency increased to $0.65^{+0.06}_{-0.06}$. Given our efficiency estimate for the receiver optics, this telescope efficiency implies a detector efficiency exceeding 0.90. The overall noise-equivalent temperature of the 90 GHz focal plane improved from $19 \mu\text{K}\sqrt{\text{s}}$ to $9.7 \mu\text{K}\sqrt{\text{s}}$.

Keywords: Cosmic microwave background radiation (322), Polarimeters (1127), Astronomical detectors (84), CMBR detectors (259)

1. INTRODUCTION

Measurements of the cosmic microwave background (CMB) have provided the tightest constraints to date on the parameters of the Λ CDM cosmological model and its extensions (e.g., Bennett et al. 2013; Hinshaw et al. 2013; Planck Collaboration et al. 2020; BICEP/Keck Collaboration et al. 2021). For the past twenty years, advances in the sensitivity of CMB measurements have been enabled in a large part by advances in cryogenic detector technology, with transition-edge-sensor (TES) bolometers playing a central role (e.g., Niemack et al. 2008; Kuo et al. 2008; Shirokoff et al. 2009; Arnold et al.

2012; Suzuki et al. 2012; Rostem et al. 2012; Appel et al. 2014; Posada et al. 2016; Hui et al. 2016). Along these lines, this paper concerns improvements to cryogenic detector performance for the Cosmology Large Angular Scale Survey (CLASS) project. CLASS aims to measure CMB polarization on the largest angular scales ($\ell < 30$) to constrain the optical depth of reionization and primordial gravitational radiation (Essinger-Hileman et al. 2014; Watts et al. 2015; Harrington et al. 2016; Watts et al. 2018). This is one of the frontiers of the CMB field, with associated projects pursuing complementary strategies (LiteBIRD Collaboration et al. 2022; Lazear et al. 2014; Addamo et al. 2021; Lee et al. 2020; Addamo et al.

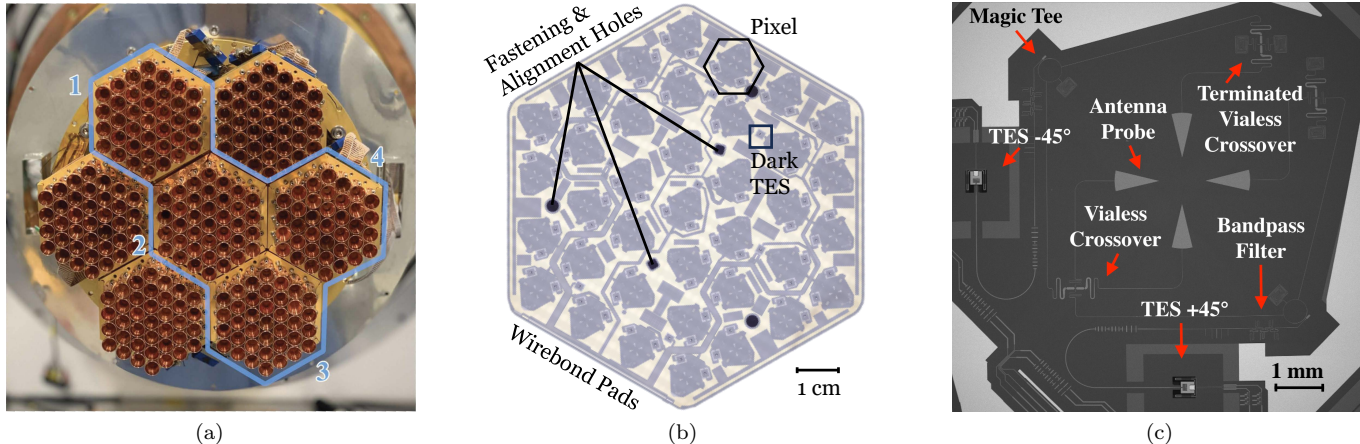


Figure 1. (a) Photograph of the upgraded 90 GHz focal plane, taken at the CLASS site. The four new modules are outlined in blue and numbered with the convention used throughout the paper. Thirty-seven copper feedhorns per module couple detectors to the incoming radiation. (b) Within each module is an indium-bonded stack of silicon wafers into which is built an integrated array of thirty-seven dual-polarization detector pixels. (c) A single pixel shows updated components: the terminated vialess crossover, the magic tee, and the TES. Images are reproduced from N22; N23.

2021; Rubiño-Martín et al. 2023; May et al. 2024). Major upcoming international-scale ground-based surveys will constrain primordial gravitational waves and measure the growth of cosmic structure on smaller angular scales (Simons Observatory Collaboration et al. 2019; CMB-S4 Collaboration et al. 2022).

Located on Cerro Toco at 5200 m in the Chilean Atacama Desert, the CLASS polarization-sensitive array of microwave telescopes operates in frequency bands centered approximately on 40, 90, 150, and 220 GHz (Eimer et al. 2012; Appel et al. 2014; Harrington et al. 2018; Dahal et al. 2018). Among these, the 90 GHz band is closest to the minimum in polarized Galactic emission (Planck Collaboration et al. 2016, Figure 51), and the nominal CLASS design has two dedicated 90 GHz telescopes. However, the initial 90 GHz detectors produced in 2018 had problematic variations in stable bias range and optical efficiency (Dahal et al. 2022, hereafter D22). To improve detector performance we updated the detector design and replaced part of the first 90 GHz telescope’s detectors with the upgraded version in August 2022. Initial characterizations of the new detectors have been reported in Núñez et al. (2022, 2023), hereafter N22; N23.

In this paper, we present the full in-lab and on-sky characterization of the upgraded 90 GHz focal plane. We discuss the design of the upgraded detector wafers in Section 2, emphasizing updates. The types of data for detector characterization are described in Section 3. Sections 4–8 cover the electrothermal TES parameters, bandpass, optical efficiency, noise performance, and stability. Finally, in Section 9 we summarize the results, while spatial variations in electrothermal properties and opti-

cal efficiency are covered in Appendix A. An index of parameters used to describe the instrumentation is in Appendix B.

2. UPGRADED DETECTORS

Figure 1a shows a photograph of the four upgraded detector modules installed in the 90 GHz focal plane in July 2022. In total, the detector array holds seven modules, and those replaced were the least-well performing modules in the original array (W1). The most apparent features of the modules in the photo are the thirty-seven copper feedhorns that couple the incoming radiation to the detector pixels inside the module (Zeng et al. 2010; Dahal et al. 2018). Visible behind the feedhorns is the gold-plated aluminum-silicon alloy interface plate (Ali et al. 2022). Mounted to the back of this plate is an indium-bonded and gold-plated stack of silicon wafers that provides broadband optical coupling, out-of-band light rejection, and thermalization for the detector wafer shown in Figure 1b. Orthogonal polarized signals received via the feedhorn are diplexed by a symmetric waveguide orthomode transducer (OMT) and then subsequently filtered and detected on-chip. The detector wafer integrates thirty-seven dual-polarization detector pixels. The multi-layer detector stack is fastened and aligned with the interface and feedhorns through micromachined holes. In addition to the seventy-four TESs associated with detector pixels (one per polarization per pixel), several optically isolated “dark” TESs are used to assess parasitic power loading. Each TES is voltage biased and read out through a pair of leads that connect to wirebond pads on one side of the wafer. Additional cryogenic module circuitry comprises shunt-resistor chips to provide

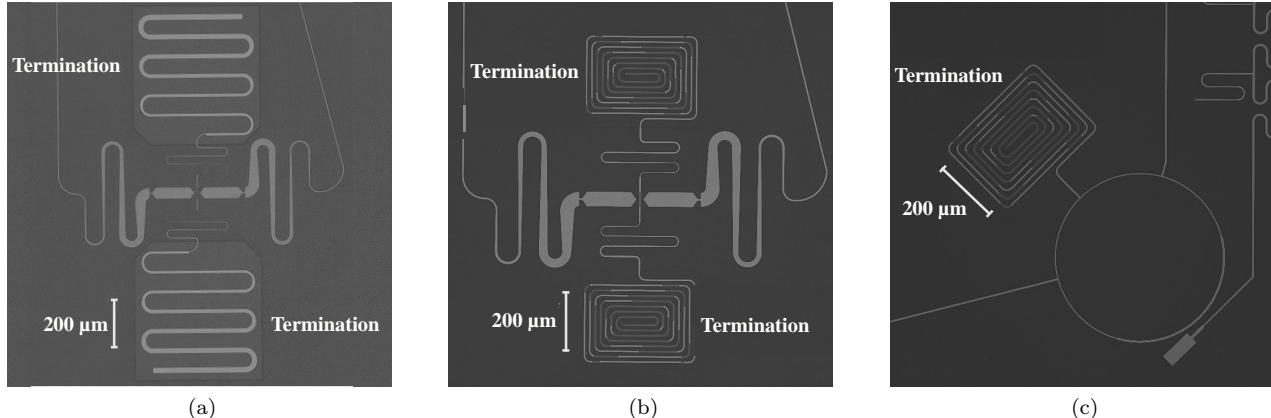


Figure 2. The terminated vialess crossover with the original (a) and updated (b) termination design together with the magic tee (c) with the updated design. In the original design, the superconducting Nb line is overlaid with a wider gold line for adiabatic absorption and impedance matching. The new termination was realized as a stepped impedance transformer from Nb to PdAu. (The light sections of the termination line are Nb while the dark sections are PdAu.) This design avoids proximitization, is robust against fabrication variability, and reduces the device footprint. Images with the revised design were adapted from N23.

voltage biases and time-division multiplexing chips to read the detector current (Reintsema et al. 2003; Doriese et al. 2016). The detector modules are controlled and read out with warm Multi-Channel Electronics (MCE) (Battistelli et al. 2008).

Figure 1c shows the upgraded detector pixel, which inherits most of its design from the original W1 detectors. For a full description of the original CLASS 90 GHz module and detector design, see Denis et al. (2009); Chuss et al. (2016); Rostem et al. (2016); Dahal et al. (2018). Here we provide an overview and highlight design elements that changed in the upgraded detectors. Aside from terminations, the microwave circuitry on the detector wafer is made from superconducting niobium with a dielectric of single-crystal silicon derived from the $5\ \mu\text{m}$ -thick device layer of a silicon-on-insulator (SOI) wafer. A pair of symmetric antenna probes couple each orthogonal polarization of incoming light arriving through a circular waveguide that runs from the base of the feedhorn through the interface plate and the initial layers of the detector wafer stack. A waveguide quarter-wave backshort behind the detector wafer enhances the coupling (Crowe et al. 2013). Transmission lines from the antenna probes transition from co-planar waveguide to microstrip transmission lines. The radiation from opposing probe antennas is then coherently combined at the magic tee, which transmits the difference and terminates the sum signal (U-Yen et al. 2008). The signal paths are symmetrized by passing through either a vialess crossover or an impedance-matched “dummy” termination (U-yen et al. 2009). The signal transmitted by the magic tee propagates through microstrip band-defining filters before terminating at the corresponding TES bolometer.

2.1. Revised Magic Tee and Crossover Terminations

For the original 90 GHz detector pixels, absorber terminations for the terminated vialess crossovers and the magic tees were realized in a microstrip configuration by overlaying a superconducting Nb line with a wider resistive Au layer shaped to provide adiabatic absorption along the structure and impedance matching. An example of this termination design is shown in Figure 2a. Due to concerns that termination performance was degraded by proximitization of the Au (Sadleir et al. 2010; Nagler et al. 2020), the terminations for the upgraded pixel were redesigned. Images of the crossover and magic tee with the new termination design are shown in Figures 2b and 2c. The new design features a stepped-impedance transformer from superconducting Nb to normal PdAu. Palladium’s larger density of states, reduced diffusivity, and strong Pauli paramagnetism combine to limit the proximitization of PdAu relative to that of Au. PdAu is a disordered alloy (RRR=1.1) with a relatively high electrical bulk resistivity, allowing a reduction in the termination footprint. Finally, the stepped-impedance design is more robust against dimensional variations and misalignments in fabrication than the original tapered design.

2.2. Revised TES Bolometer Thermal Circuit

Figure 3 shows the TES bolometer in detail. The signal enters by the tapered Nb microstrip in a waveguide channel. This transmission line crosses a short Si beam, which dominates the thermal conductance between the bolometer and the rest of the detector wafer (Rostem et al. 2014). (The long, folded legs that carry the voltage bias do not add significantly to the thermal conduction.) The short Si beam, which is made from the same de-

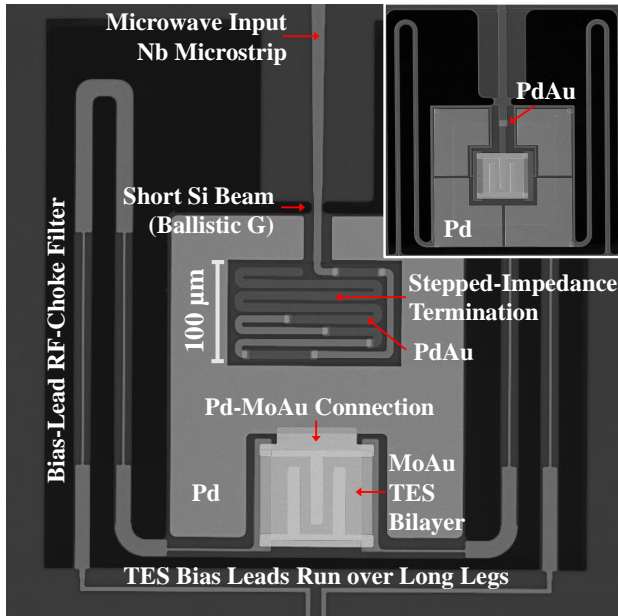


Figure 3. The 90 GHz TES Bolometer. (Main Image) The TES was revised to include (1) an Nb-PdAu stepped-impedance termination, (2) an single Pd film for thermal mass, (3) a direct normal-metal contact between the MoAu TES and the Pd, and (4) a revised bias-lead filter circuit implementation extending RF chokes onto the bias-lead legs. This image was reproduced from N23. (Top-Right Inset) The original TES used a left-right symmetric, distributed quarter-wave backshort termination with PdAu absorber. This image was reproduced from Dahal et al. (2018).

vice layer as the stripline dielectric, is $5 \mu\text{m}$ thick. The width of the beam was targeted (measured) to be $10 \mu\text{m}$ ($9.5\text{--}9.7 \mu\text{m}$), which was chosen to provide 13.2 pW of cooling at the target TES critical temperature and the bath temperature. The short Si beam and bias-lead legs suspend the TES island, which is also $5 \mu\text{m}$ thick being built from the device layer. On this island are the Pd thermal mass, the MoAu superconducting bilayer, and the TES termination. The TES was designed to operate at a critical temperature of $T_c = 190 \text{ mK}$. This increase over the original design’s $T_c = 150 \text{ mK}$ was to accommodate additional bias power range, matching the more stable 150/220 GHz detectors (Dahal et al. 2020). The rest of the detector wafer is maintained at a bath temperature T_{bath} of approximately 50 mK by the helium dilution refrigerator-based receiver (Iuliano et al. 2018).

On the TES island, the Pd thermal mass provides the majority of the heat capacity. In the original design (inset of Figure 3), four distinct Pd regions define a distributed sensor heat capacity and additionally provide the low-impedance sections of the bias choke. In the revision, the four distinct Pd regions were replaced with a unified, contiguous film that primarily serves to set the heat

capacity of the TES. To obtain a target heat capacity of 3.7 pJ/K at $T_c = 190 \text{ mK}$, an area of $45945 \mu\text{m}^2$ of Pd was deposited to a thickness of 400 nm .¹

The MoAu bilayer is the same as in the original design, incorporating the “zebra-stripe” normal-metal meander that helps stabilize the TES (Staguhn et al. 2004; Ullom et al. 2004). Unlike the original, the upgraded design incorporates an additional metallic contact extending the zebra stripes to the Pd. This contact further unifies the thermal circuitry of the island, lumping the electronic heat capacity into a single element.

2.3. Revised TES Bolometer Termination

The bolometer signal termination was revised to incorporate a stepped-impedance Nb-PdAu termination similar to that used for the magic tee and crossover, whereas the original bolometer (inset of Figure 3) used a distributed quarter-wave short and a sub-wavelength PdAu resistive line for signal termination. The decision to transition to the stepped-impedance design allowed the same basic modeling approach to be used for the TES, magic tee, and crossover terminations, and it addressed concerns about sensitivity of the prior design to misalignment and membrane stresses, described below.

2.3.1. Design of Original Termination

Electromagnetic modeling of this structure needs to be carried out in three dimensions including the surrounding cavity, which has three openings (hereafter called “ports”) – one for the incoming microstrip carrying optical power and two for the bias leads traveling to the bolometer island (top-middle, bottom-left, and bottom-right in Figure 3). Modeling of the original TES cavity used the mirror symmetry of the structure to reduce the simulation volume, allowing consideration of only two ports: the signal input and one of the bias leads. This is valid as long as the bolometer island remains planar and there is no misalignment in bonding the backshort with the detector wafer. While the microwave input at the top of Figure 3 drives the TES cavity symmetrically, bowing of the TES bolometer structures due to membrane stresses or misalignment of elements in hybridization of the TES enclosure can potentially break this symmetry. Differential modes in the structure are not captured in the symmetric simulation. Only symmetric modes in which waves are in phase between the bias ports would appear in the model. Microwave power from differential modes is not absorbed on the bolometer island, reducing optical coupling efficiency.

¹ This assumes a Pd specific heat of 9.4 mJ/mol/K^2 from Kittel (1996).

This approach largely followed the successful simulation strategy used in modeling the inputs and readout signals for the 40 GHz sensor, where the wavelength is relatively large compared with the cavity dimensions. Because the size of the enclosing cavity for the TES bolometer is set mostly by the thermal circuit, it remains the same between frequency bands. The smaller wavelength for the 90 GHz and 150/220 GHz detectors compared with the cavity dimensions made this aspect of the design more challenging. In reviewing the sensitivity of the CLASS 150/220 GHz pixel design with the electromagnetic simulations it was realized that the mirrored, 2-port model suppressed coupling to differential modes in the bias circuit. The model was refined to treat the integrated circuit and its packaging structures as a full 3-port structure. This model was used to confirm that excitation of the cavity did not lead to trapped mode resonances (Morgan & Pan 2013) that could cause a loss of efficiency. The 150/220 GHz detector circuitry and its enclosure successfully addressed these considerations through the arrangement of the circuitry within the cavity (Dahal et al. 2020) and changes to the bias line filtering detailed below.

2.4. Voltage Bias Line Routing and Filtering

The routing and filtering of the TES bias leads were revised in the upgraded design. In the original bias filter design, the structure resided on the TES island. The new bias filter spans the long, folded legs from the bolometer island to the cavity wall. In addition, the revised design has a larger stop-band (U-yen & Wollack 2008) and works in concert with the TES cavity enclosure as one of several means of mitigating potential blue-leak radiation threats.

3. DATA

Several datasets were used to characterize the upgraded 90 GHz detectors. In-lab non-optical (“dark”) data were used to measure several basic electrothermal parameters (Section 4) and phonon noise (Section 7). In-lab optical data were used to measure the passbands (Section 5). Based on cosmological survey data taken from August to October 2022, we estimated optical time constants (Section 4) and noise spectra (Section 7) for 10-minute data packages. From the survey data, we removed packages for which (1) detectors had anomalous optical response (as indicated by an unusual polarization modulator emission signal), (2) the noise equivalent power (NEP) fluctuated significantly over a contiguous span of data (< 24 hours), (3) wind speeds exceeded 6 m s^{-1} , or (4) optical loading was unusually low ($P_\gamma < 3.8 \text{ pW}$) or high ($P_\gamma > 5.5 \text{ pW}$). We also excluded all detectors that did not have an

orthogonally polarized counterpart (i.e., “unpaired” detectors).² This selection of the survey data is meant to best capture the essential characteristics of the upgraded detectors and some aspects of the receiver (e.g., optical efficiency) rather than characterize the performance of the instrument throughout the survey and under all conditions that will ultimately affect CLASS polarization maps. Finally, we derived optical efficiencies (Section 6) from observations of Jupiter carried out in the austral spring of 2022 (N23).

4. ELECTROTHERMAL PARAMETERS

In this section we present in-lab and on-sky measurements of the electrothermal properties of the upgraded TES bolometers. Table 1 shows a summary of the parameters. In addition, Appendix B contains an index of parameters and relevant equations. Preliminary values, derived from in-lab measurements, were reported in N22. To these results, we append measurements of the optical time constant (τ_γ), thermal time constant (τ), and heat capacity (C). Figure 4 shows the distributions of these parameters for the upgraded wafers relative to their per-wafer median values given in Table 1. In Appendix A, we explore the spatial distribution of these properties across the wafer. As we shall see, the measured values of several device properties diverge from their design targets. In Section 4.4 we explore alternative measurement and theory scenarios that could explain these discrepancies. Fortunately, the properties most critical to detector performance, such as saturation power, noise power, optical efficiency, optical time constant, and stability, are scenario independent.

4.1. Normal Resistance and Saturation Power

Several of these parameters were derived using “ I - V curves” showing the TES current (I_{TES}) as a function of TES voltage (V_{TES}). The voltage bias is ramped down in steps, driving the TES from a normal resistor state to a superconducting state. We convert from the output MCE digital-to-analog feedback units and voltage bias to I_{TES} and V_{TES} following § 4.1 of Appel et al. (2022). The normal resistance of the TES (R_N) is given by the inverse slope of the normal branch of the I - V curve. The saturation power (P_{sat}) is the approximate optical loading above which the TES biased on its superconducting transition is driven normal. We estimate the saturation power as the amount of bias power ($P_J = I_{\text{TES}} \times V_{\text{TES}}$)

² Estimating detector NEP using the difference of data from two orthogonally-polarized paired detectors mitigates contributions from noise common to the pair. However, we have found that such common-mode noise does not impact sensitivity estimates at 90 GHz (Cleary 2023).

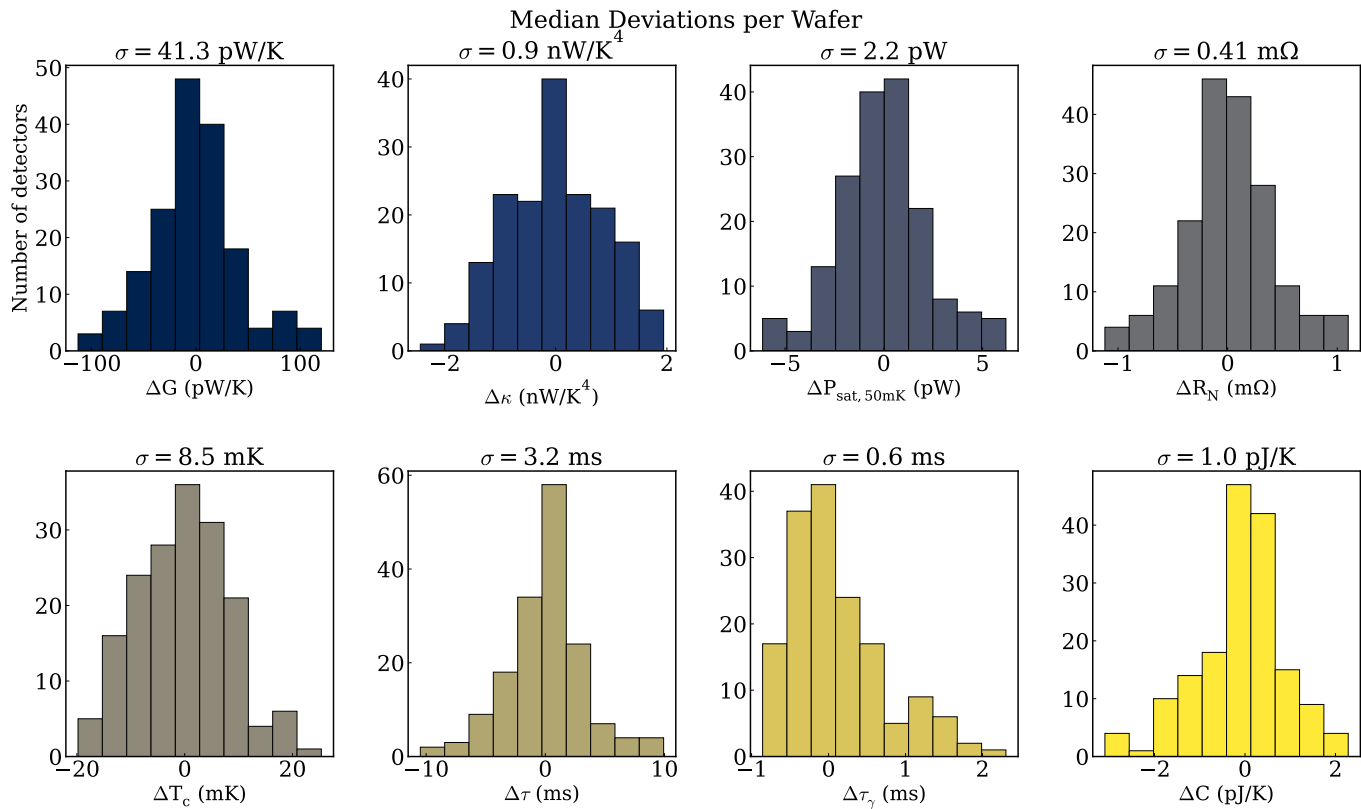


Figure 4. Distributions of TES electrothermal parameters relative to their per-wafer median value: thermal conductance (G), prefactor (κ), saturation power for $T_{\text{bath}} = 50$ mK (P_{sat}), normal resistance (R_N), critical temperature (T_c), thermal time constant (τ), optical time constant (τ_γ), and heat capacity (C). Estimation of these parameters is described in Section 4. Outliers beyond 3σ from the per-wafer median of the underlying distributions have been excluded. Subplot titles show the standard deviation of the histograms. Per-wafer median values for all parameters are given in Table 1. These distributions can be compared to previously published results for the original W-band array (Figure 7 in Dahal et al. (2018)) and the Q-band array (Figure 4 in Appel et al. (2014)). The TES parameters in the upgraded W-band wafers show greater uniformity than those in the original wafers but do not match the consistency achieved by selecting individual pixels from Q-band wafers.

required to maintain the TES at its superconducting critical temperature with a resistance equal to 70% R_N with no radiative load (dark configuration). Except when otherwise stated, P_{sat} will refer to the saturation power for the lowest possible $T_{\text{bath}} = 50$ –60 mK.³ Table 1 shows that we measured $P_{\text{sat}} = 8$ –12 pW for the upgraded detectors. This is $\sim 30\%$ below the target of 13.2 pW. Figure 4 shows that within a module, the saturation powers vary with standard deviation ± 2.2 pW about the median. In Appendix A we discuss how this variation takes the form of gradients across the wafers as opposed to spatially random distributions.

³ For the critical temperatures considered here, $T_c = 150$ –190 mK, the fractional change in P_{sat} in the range $T_{\text{bath}} = 50$ –60 mK is $\sim 1\%$, well below uncertainties.

4.2. Critical Temperature and Thermal Conductivity

Using the same I – V curve approach described above, we measured saturation powers $P_{\text{sat},i}$ corresponding to a wide range of bath temperatures $60 \text{ mK} < T_{\text{bath},i} < 250 \text{ mK}$ (N22). With these measurements, we simultaneously determined T_c and the thermal-conductance prefactor κ using the relation (Irwin & Hilton 2005):

$$P_{\text{sat},i} = \kappa (T_c^n - T_{\text{bath},i}^n). \quad (1)$$

In keeping with the assumption that the short Si beam connecting the TES to the bath operates in the ballistic phonon limit, we assumed $n = 4$. From Table 1 we see that the median critical temperatures for the upgraded modules were measured to be $T_c = 150$ –170 mK, about 15% lower than the target of $T_c = 190$ mK. Because $P_{\text{sat}} \propto T_c^n$, the lower T_c implies a $\sim 50\%$ -lower saturation power, all other parameters being on target. Given that saturation power is only $\sim 30\%$ below the target implies that the prefactor κ is higher than designed

Table 1. Electrothermal Parameters

	Upgraded Wafers					Target	Original Array ^a
	1	2	3	4	Total		
Thermal Conductance G [pW/K]	269 ⁺⁶² ₋₄₄	229 ⁺²⁵ ₋₂₇	257 ⁺²⁷ ₋₄₅	304 ⁺⁴⁶ ₋₅₃	255 ⁺⁵⁵ ₋₄₂	280	452
Thermal Conductance Prefactor κ [nW/K ⁴]	16.1 ^{+0.64} _{-0.72}	16.9 ^{+1.2} _{-1.0}	13.9 ^{+1.0} _{-0.94}	15.2 ^{+0.83} _{-0.98}	15.2 ^{+0.83} _{-0.98}	10	24.9
Saturation Power P_{sat} [pW]	10.7 ^{+3.3} _{-2.1}	8.4 ^{+1.5} _{-1.3}	10.7 ^{+1.4} _{-2.6}	12.7 ^{+2.6} _{-2.5}	10.1 ^{+3.1} _{-2.3}	13.2	18.4
Normal Resistance R_N [m Ω]	12.7 ^{+0.5} _{-0.3}	11.0 ^{+0.5} _{-0.6}	10.2 ^{+0.2} _{-0.3}	10.7 ^{+0.4} _{-0.3}	10.8 ^{+1.8} _{-0.6}	12	11.0
Critical Temperature T_c [mK]	163 ⁺¹⁰ ₋₇	151 ⁺⁸ ₋₁₀	165 ⁺⁸ ₋₁₂	171 ⁺⁶ ₋₇	161 ⁺¹² ₋₁₀	190	167
Thermal Time Constant τ [ms]	17.3 ^{+4.3} _{-2.9}	15.8 ^{+2.2} _{-3.9}	17.0 ^{+2.0} _{-2.5}	12.6 ^{+3.0} _{-3.8}	16.0 ^{+2.8} _{-4.6}	13.2	7
Optical Time Constant τ_γ [ms]	3.5 ^{+0.8} _{-0.3}	4.7 ^{+1.4} _{-0.6}	4.6 ^{+1.9} _{-0.4}	3.2 ^{+1.3} _{-0.3}	4.2 ^{+1.0} _{-0.9}	–	2.1
Heat Capacity C [pJ/K]	4.8 ^{+1.2} _{-1.1}	3.8 ^{+0.5} _{-1.2}	4.5 ^{+0.6} _{-1.3}	3.8 ^{+1.2} _{-1.0}	4.1 ^{+0.9} _{-1.2}	3.7	4

NOTE—Median values and 68% intervals of key electrothermal parameters for the four upgraded wafers (numbered as shown in 1a) and the originally deployed W1 array. The “Total” column shows the median values across the four upgraded wafers, and the “Original Array” column shows the median values across the full seven-wafer array that was originally deployed.

^aValues reported in D22. P_{sat} values published therein were calculated at 80% R_N , and 70% R_N in this work. For the upgraded detectors the measured P_{sat} drops by $\sim 2\%$ when calculated at 70% R_N compared to 80% R_N .

(though see Section 4.4). The prefactor κ is a function of the geometry of the short Si beam (Figure 3, Rostem et al. 2014). Table 1 shows that the measured P_{sat} and T_c imply prefactors in the range $\kappa = 14\text{--}17\text{ nW K}^{-4}$ compared to the design value of 10 nW K^{-4} . Figure 4 shows that within a wafer, the standard deviation of the κ values is small, approximately 0.9 nW K^{-4} , so the discrepancy between the measured value and the design value cannot be attributed to a statistical fluctuation in the measurement. Finally, the thermal conductance (G) of the TES is given by (Irwin & Hilton 2005):

$$G = \left. \frac{dP}{dT} \right|_{T_c} = n\kappa T_c^{n-1}. \quad (2)$$

Because $T_c^n \gg T_{\text{bath}}^n$, the thermal conductance is well approximated as $G \approx nP_{\text{sat}}/T_c$. Therefore, we would expect the measured G to be approximately 10% low compared to the design target. This is indeed the case with measured values $G = 230\text{--}300\text{ pW/K}$ versus the designed 280 pW/K . Figure 4 shows that the range of values per wafer has a standard deviation of 41.3 pW/K .

4.3. Time Constants and Heat Capacity

To measure the on-sky optical time constant (τ_γ), we fit for the single-pole filter that minimizes the hysteresis of the periodic modulator emission signal in the TODs, as in Appel et al. (2019). Table 1 shows that the median τ_γ per wafer lies in the range 3–4 ms. This time constant is shorter than the thermal time constant ($\tau = C/G$) due to electrothermal feedback. The speed up increases with both bias power P_J and the logarithmic derivative of resistance with respect to temperature (α) (Irwin & Hilton 2005). Figure 5 shows τ_γ as a function of optical loading (P_γ). Because $P_{\text{sat}} = P_\gamma + P_J$, an increase in optical loading results in a decrease in bias power. This decreases the electrothermal feedback, which results in a longer optical time constant, consistent with the trend of increasing τ_γ with increasing P_γ in Figure 5.

Appel et al. (2022) describes how to use detector responsivity measurements (derived from I – V curves) to obtain the thermal time constant τ from the optical time constant τ_γ . (See Equation 26 of Appel et al. 2022 and associated discussion for details.) Applying this formalism, Table 1 shows that we found median thermal time constants in the range $\tau = 13\text{--}17\text{ ms}$. Combining this result with measured thermal conductivities gives

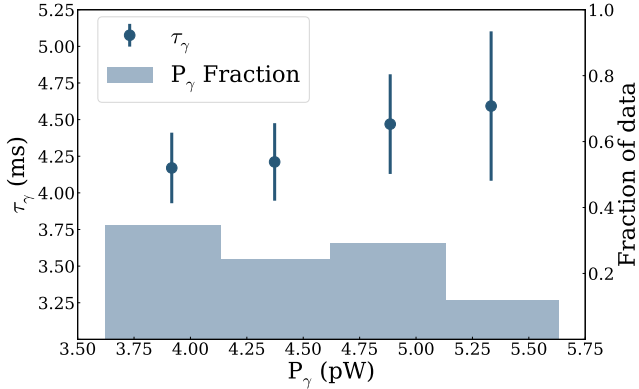


Figure 5. The optical time constants of the upgraded detectors as a function of optical loading P_γ . Increasing optical loading results in a decrease in bias power and therefore electrothermal feedback. The drop in feedback is consistent with the marginal trend of slowing of the detectors with increasing P_γ .

median heat capacities per wafer in the range $C = 3.8$ – 4.8 pJ/K (Table 1) with an RMS variation per wafer of $\sigma_{\Delta C} = 1$ pJ/K (Figure 4). As discussed in Section 2, the TES heat capacity is dominated by the 400 nm-thick Pd covering most of the TES island. The heat capacity of the design listed in Table 1 (3.7 pJ/K) was computed for the target $T_c = 190$ mK. Because the heat capacity of normal metals is proportional to temperature, the expected heat capacity for the measured $T_c = 160$ mK is revised downwards to $C \approx 3.1$ pJ/K. Therefore, the measured heat capacity estimate is higher on average by approximately 1 pJ/K than the expectation. In the next section, we investigate whether systematic errors in the measurements or deviations in the assumptions presented above can reconcile discrepancies between our baseline parameter estimates and the design targets.

4.4. Alternative scenarios

In the previous section, we found a discrepancy between the measured and targeted thermal conductance prefactor κ , which is in principle a function of the dimensions of the short mono-crystalline Si beam connecting the TES island to the rest of the detector wafer. We also measured an elevated heat capacity relative to that expected from the 400 nm-thick Pd layer covering most of the island. In this section, we explore two alternative scenarios and whether they could reconcile the measured values with the design targets.

First, we consider what changes if we relax the assumption that ballistic photon transport dominates the thermal conductance across the short Si beam. Non-idealities would result in $n < 4$ in Equations 1 and 2. Because P_{sat} is measured by the bias power under dark condi-

tions, it is independent of the model assumptions. Given that $P_{\text{sat}} \approx \kappa T_c^n$ and $T_c < 1$, decreasing n would require decreasing κ . Setting $n = 3.77$ would shift the average measured κ from 15.2 nW/K⁴ to the target 10 nW/K⁴.⁴ Therefore relaxing the assumption on n can resolve the κ discrepancy. Unfortunately, it cannot simultaneously explain why the estimated heat capacity is 25% above expectation. As described in Section 4.3, we estimated the heat capacity from measurements as $C = \tau G$. The thermal conductivity $G \approx n P_{\text{sat}} / T_c$, meaning the 5% decrease in n considered here would marginally reduce the C discrepancy. The thermal time constant τ is to first order inversely dependent on n through G (Appel et al. 2022), canceling some of these gains.

Second, we consider whether a systematic error in the measurement of T_c could resolve the discrepancies. Variations between thermometers on different detector modules during I – V curve measurements would allow for approximately 10 mK systematic error. As in the previous paragraph, we take $P_{\text{sat}} \approx \kappa T_c^n$ to be a fixed, measured quantity. Therefore, if the measured T_c were below the actual T_c , then the measured κ would be higher than the actual κ , a change that would bring the actual κ into better agreement with the design value. If the critical temperature were $T_c \approx 170$ mK instead of the measured ~ 160 mK, then the inferred κ would shift to $\kappa \approx 12$ nW/K⁴, reducing the discrepancy from the target value from 50% of the expected value to 20%. Next, we consider what a 10 mK increase in T_c would mean for the discrepancy between measured (4.1 pJ/K) and expected (3.1 pJ/K) heat capacity. Because the heat capacity of metals increases linearly with temperature, the expected heat capacity would increase to approximately 3.3 pW/K. If we treat the thermal time constant τ as a measured, fixed quantity, then the heat capacity inferred from measurements $C = \tau G = \tau(n P_{\text{sat}} / T_c)$ would decrease to approximately 3.9 pW/K. Therefore, the discrepancy between measured and expected heat capacity decreases from 30% of the expected value to 15%. In summary, a +10 mK shift in critical temperature significantly reduces the discrepancies between the design targets and measured T_c , κ , and C . As an aside, measurements of noise (Section 7) do not strongly constrain T_c given a fixed P_{sat} : our noise measurements can accommodate either $T_c = 160$ mK or $T_c = 170$ mK. One final observation that is consistent with $T_c = 170$ mK: after depositing the TES MoAu bilayer, “witness” samples deposited along side the detectors yielded $T_c = 165$ – 182 mK. These

⁴ Unfortunately, the n and κ parameters are significantly covariant in a simultaneous fit to IV data, so we are restricted to fixing n and fitting for κ or vice-versa.

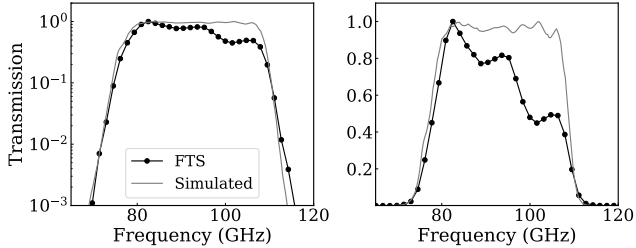


Figure 6. Bandpass FTS measurement and simulation. On the left in logarithmic scale and on the right in linear scale. The measured bandpass edges agree well with the simulation. In the text, we present arguments that the decrement in transmission on the high-frequency half of the bandpass is a measurement artifact.

were measured in a four-wire configuration at NASA, independently from other measurements described here. However, the TES bilayers undergo further processing, including the addition of the gold meander and niobium leads, that could change the average T_c of the finished TESs from that of the witness samples. In particular, film stress is likely to be a major factor in T_c change with the T_c of a TES changing between a solid frame and a released membrane.

In summary, having a lower n or a higher T_c are alternative scenarios that bring the κ inferred from measurements into better agreement with the design. And the T_c adjustment is more effective at solving the discrepancy for heat capacity. Of course, the reality is likely a more general scenario that combines deviations in κ , T_c , and n from the baseline assumptions of Section 4. Regardless, the key observational parameters— P_{sat} , NEP/NET, η , τ , etc.—are measured values and independent of the model assumptions.

5. BANDPASS MEASUREMENTS

Bandpass measurements were made using a Fourier Transform Spectrometer (FTS) utilizing a polarizing Martin-Puplett interferometer (Wei 2012). The FTS has a movable mirror that sweeps through a 150 mm range at 0.5 mm/s, resulting in a resolution of ~ 1.6 GHz. The input signal of the FTS is a wide-band thermal source with a temperature of $\sim 1000^\circ\text{C}$. The output signal of the FTS, measured by the detectors, is modulated with a chopper at 21 Hz. The bandpass is given by the real component of the Fourier transform of the interferogram.

The measured response plotted in Figure 6 is the inverse-variance-weighted average over 93 bolometers that yielded high-quality interferograms and bandpasses across wafers 1, 2, and 3.⁵ We also simulated the band-

pass for the upgraded detector architecture using Ansoft HFSS.⁶ The measured bandpass edges are in good visual agreement with the simulation; the data, however, show an approximately 50% decrement of power in the upper section of the band, especially above 100 GHz. Measurements made with a second FTS did not show this decrement (Pan et al. 2019). (An observed ± 1 GHz systematic error in our frequency calibration of the second FTS made it less reliable for determining the absolute values for bandpass edges.) Furthermore, the power measured from Jupiter (Section 6) is too high if the smaller bandwidth implied by the measurement is assumed. Therefore, we conclude that discrepancies observed in-band between measured and simulated responses are likely due to optical effects related to the test setup.

In Table 2 we report bandwidths and effective bandcenters for diffuse sources for the simulated bandpass and the measurement shown in Figure 6. These are computed following the definitions in Section 3.1 of D22. Uncertainties for the bandwidths (effective center frequencies) are given by the summation in quadrature of the standard errors on the mean and the FTS measurement resolution (half FTS measurement resolution). Due to the likely-artificial power suppression in the measurement, the simulated bandwidths and bandcenters are preferred over the measured quantities.

Before integration into the CLASS detector modules, each 37-pixel detector wafer is hybridized into a stack of silicon wafers. The overall design safeguards against the detection of out-of-band radiation (a.k.a., “blue leak”, for the common case that the spurious signal is at higher frequency). These safeguards include a photonic choke etched into the wafer that contacts the CLASS module’s interface plate to the feedhorns, an indium-sealed degenerately-doped silicon back-short cap that shields the detector circuitry after the antenna probes, and RF filtering on the bias leads of the TES (Denis et al. 2009; Rostem et al. 2016; Dahal et al. 2018). As was found with previous generations of CLASS detectors, the upgraded detectors show good suppression of power outside the passband: FTS measurements in the range 40–300 GHz place an upper limit on out-of-band power at 0.7% of the in-band response.

6. OPTICAL EFFICIENCY IMPROVEMENTS

We report telescope optical efficiency improvements based on observations of Jupiter. A full description of the

⁵ Wafer 4 was not delivered in time for the FTS measurement.

⁶ ANSYS 2019 R1, <https://www.ansys.com/products/electronics/ansys-hfss>

Table 2. Bandpass Parameters

Parameter	Simulated	Measured
	(GHz)	(GHz)
Bandwidths		
Full-Width Half-Power	31.4 ± 1.8	21.5 ± 1.8
Dicke	33.9 ± 1.7	32.0 ± 1.7
Effective Bandcenters		
CMB	92.4 ± 0.9	90.8 ± 0.9
Dust	94.2 ± 0.9	92.7 ± 0.9
Rayleigh–Jeans	92.8 ± 0.9	91.2 ± 0.9
Synchrotron	89.8 ± 0.9	88.9 ± 0.9

NOTE— For reasons given in the text, we consider bandcenters and bandwidths computed from the simulated bandpass as more reliable. Measured values were previously reported in N23.

Jupiter observations is given in N23. In summary, optical efficiencies were measured by comparing the observed and expected amplitudes of Jupiter in the Rayleigh–Jeans limit, given by:

$$A_J = k_B T_J \Delta\nu B_{\text{dil}}, \quad (3)$$

where k_B is the Boltzmann constant, T_J is the Jupiter brightness temperature at 90 GHz (172.8 K) as reported by the WMAP team (Bennett et al. 2013), $\Delta\nu$ is the observing bandwidth of 31 GHz (consistent with the FWHP of the simulated bandpass in Table 2), and B_{dil} is the beam dilution factor given by the ratio of the oblateness-corrected solid angle of Jupiter (Ω_J) over the convolution of the detector beam with Jupiter (Ω_B).

The telescope optical efficiency⁷ denoted by η is given by the ratio of the measured amplitude A_{obs} with the expected amplitude A_J :

$$\eta = \frac{A_{\text{obs}}}{A_J} = \frac{A_{\text{obs}} \Omega_B}{k_B \Delta\nu T_J \Omega_J}. \quad (4)$$

The distribution of telescope optical efficiencies of the currently fielded detectors is shown in Figure 7. Table 3 gives the median optical efficiency and 68% confidence region for each upgraded wafer, for the four upgraded wafers together, and for the full detector array with

⁷ Telescope optical efficiency is the product of detector efficiency with the absorption and spillover efficiency of the telescope. Unless otherwise specified, abbreviations “optical efficiency” and “efficiency” refer to this quantity.

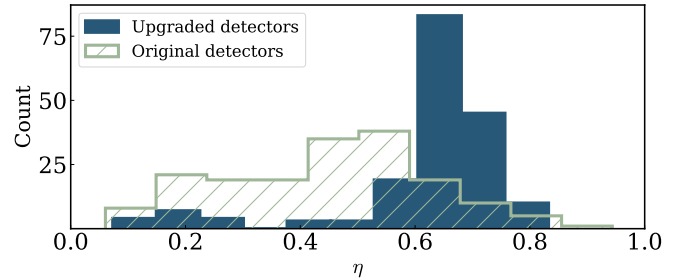


Figure 7. Telescope optical efficiencies for the 353 detectors in the upgraded array with optical efficiencies above 5%. The upgraded detectors provide higher optical efficiency compared to their original counterparts in the upgraded array. (The originals, not included here, that were replaced by the upgraded detectors had poorer performance than those that were retained.) Of the sixteen upgraded detectors with optical efficiencies below 0.4, eleven come from wafer 1, which had fabrication issues that were improved for wafers 2–4.

seven wafers. The optical efficiency across all upgraded detectors is 0.65 ± 0.06 . Iuliano (2020) estimated the efficiency of the 90 GHz receiver optics accounting for only spill to be 0.78, and 0.58 when also including absorption and reflection. The absorption in cryogenic filters and lenses was likely overestimated. A plausible scenario consistent with the upgraded detector telescope optical efficiency of 0.65 includes spill efficiency of 0.78, detector efficiency of 0.91, and telescope absorption and reflection efficiency of 0.91. By contrast, Figure 7 shows that the original detectors retained in the upgraded array have a broader distribution of optical efficiencies with a lower median. Altogether, the efficiencies for original and upgraded detectors in the upgraded array are distributed as $0.60^{+0.10}_{-0.32}$. This is an improvement compared with the original array, which had optical efficiencies distributed as $0.42^{+0.15}_{-0.22}$ (Table 3, D22).

Not included in Figure 7 are detectors with optical efficiencies below 5%. Conversely, the fraction of detectors with $\eta > 0.05$ defines the detector yield, which is given in Table 3. The table shows that, although the upgraded design improved the efficiency of yielded detectors, the yielded fraction of the upgraded wafers (66%) did not significantly improve over that of the original array (62%). Based on electrical and visual inspections of the detectors, we believe the low detector yield for the upgraded wafers is likely due to open and short circuits along the bias leads extending from the detector pixels to the bondpads at the edge of the wafer. For a detailed look at the spatial distribution of detector yield, see Figure 11 of Appendix A.

Finally, in Figure 8, we present a comparison of optical efficiencies between the paired $\pm 45^\circ$ polarized detectors within a pixel. This comparison for the original detec-

Table 3. Optical Efficiency, Yield, and Noise Performance

	Upgraded Wafers					Target	Upgraded Array	Original Array ^a
	1	2	3	4	Total			
Telescope Optical Efficiency η	$0.61^{+0.07}_{-0.40}$	$0.67^{+0.03}_{-0.04}$	$0.66^{+0.06}_{-0.05}$	$0.63^{+0.08}_{-0.10}$	$0.65^{+0.06}_{-0.06}$	0.53	$0.60^{+0.10}_{-0.32}$	$0.42^{+0.15}_{-0.22}$
Detector Yield ^b	42 (57%)	51 (69%)	48 (65%)	37 (50%)	178 (60%)	80%	344 (66%)	319 (62%)
Detector NEP _{dark} [aW√s]	$12.2^{+2.8}_{-1.1}$	$11.7^{+2.2}_{-1.6}$	$11.9^{+2.6}_{-1.4}$	$13.2^{+4.2}_{-1.6}$	$12.3^{+3.3}_{-1.6}$	–	–	24
Detector Total NEP [aW√s]	$32.9^{+7.8}_{-8.8}$	$32.4^{+9.8}_{-4.1}$	$35.1^{+5.8}_{-2.5}$	$35.9^{+4.9}_{-6.6}$	$34.2^{+7.6}_{-5.8}$	–	$34.6^{+9.9}_{-6.0}$	47
NET [μ K√s]	165^{+314}_{-13}	149^{+9}_{-8}	160^{+12}_{-8}	166^{+21}_{-18}	158^{+21}_{-12}	–	9.7	19

NOTE—NEP, NET, and optical efficiency values are given as the median for single detectors with associated 68% intervals. The exceptions are the NET values in the “Array” columns, which are the sensitivities associated with the inverse variance weighted average across all detectors in the arrays.

^aValues for the original array are from Table 3 of D22.

^bThere are a maximum of 74 detectors per wafer. The “Total” and “Array” columns have maximums of 298 and 518, respectively.

tors was previously published in Figure 7 of Datta et al. (2024). Because paired detectors are colocated within a square centimeter on a wafer, it is unlikely that discrepancies in optical coupling between paired detectors arise due to variations in fabrication that are more pronounced between wafers or across the full area of a wafer. More likely, intra-pair discrepancies arise due to a design’s susceptibility to the more modest variation in depositions, lithography, and stress/strain on the TES membrane. We note that the lowest efficiency detectors (also visible in Figure 7) reside on wafer 1, which suffered from fabrication issues that were improved for wafers 2–4.⁸

7. NOISE PERFORMANCE

We quantify the noise performance by measuring the noise-equivalent power (NEP). The total detector NEP is the quadrature sum of contributions from the incoming light (NEP_γ) and from all other sources (NEP_{dark}):

$$(\text{NEP})^2 = (\text{NEP}_\gamma)^2 + (\text{NEP}_{\text{dark}})^2. \quad (5)$$

NEP_{dark} is determined in lab by measuring noise spectra with the cryostat in a dark configuration. In-lab measurements yielded a median NEP_{dark} of 12.3 ± 3.3 aW√s (N22). NEP_{dark} consists of contributions due to phonon noise, SQUID noise, and Johnson noise. For the CLASS 90 GHz detectors, NEP_{SQUID} ≈ 3 aW√s, and

NEP_{Johnson} is suppressed due to electrothermal feedback. NEP_{phonon} is given by:

$$\text{NEP}_{\text{phonon}} = \sqrt{2k_B T_c^2 G F_{\text{link}}}. \quad (6)$$

In the case of ballistic phonon transport, F_{link} is given by $(1 + (T_{\text{bath}}/T_c)^{n+1})/2$ (Boyle & Rodgers 1959). For CLASS, $T_{\text{bath}} \approx 50$ mK and $F_{\text{link}} \approx 1/2$. Using the median $T_c = 160$ mK and $G = 255$ pW K^{−1} for the four upgraded wafers, we find NEP_{phonon} ≈ 9.5 aW√s. In the allowed alternative scenario of $T_c = 170$ mK explored in Section 4.4, the predicted NEP_{phonon} is increased by only a few percent because NEP_{phonon} $\propto \sqrt{P_{\text{sat}} T_c}$, with P_{sat} being a fixed, measured quantity. Therefore the fact that the median measured NEP_{dark} is higher than predicted by the electrothermal parameters favors neither the nominal nor alternative scenarios, and there is likely some undetermined additional contribution to NEP_{dark}.

CLASS detectors are background-noise limited, i.e., the total NEP is dominated by the optical loading contribution. The photon NEP can be modeled as:

$$(\text{NEP}_\gamma)^2 = h\nu_0 P_\gamma + \frac{P_\gamma^2}{\Delta\nu}, \quad (7)$$

where h is Planck’s constant. Combining Equations 5 and 7, the total NEP is:

$$(\text{NEP})^2 = (\text{NEP}_{\text{dark}})^2 + h\nu_0 P_\gamma + \frac{P_\gamma^2}{\Delta\nu}. \quad (8)$$

We computed the total NEP using 10-minute chunks of time-ordered data (TOD) from the dataset described in

⁸ Fabrication issues included four broken membranes, wiring shorts, and a problem with the liftoff process for the magic tee and dummy cross-over terminations.

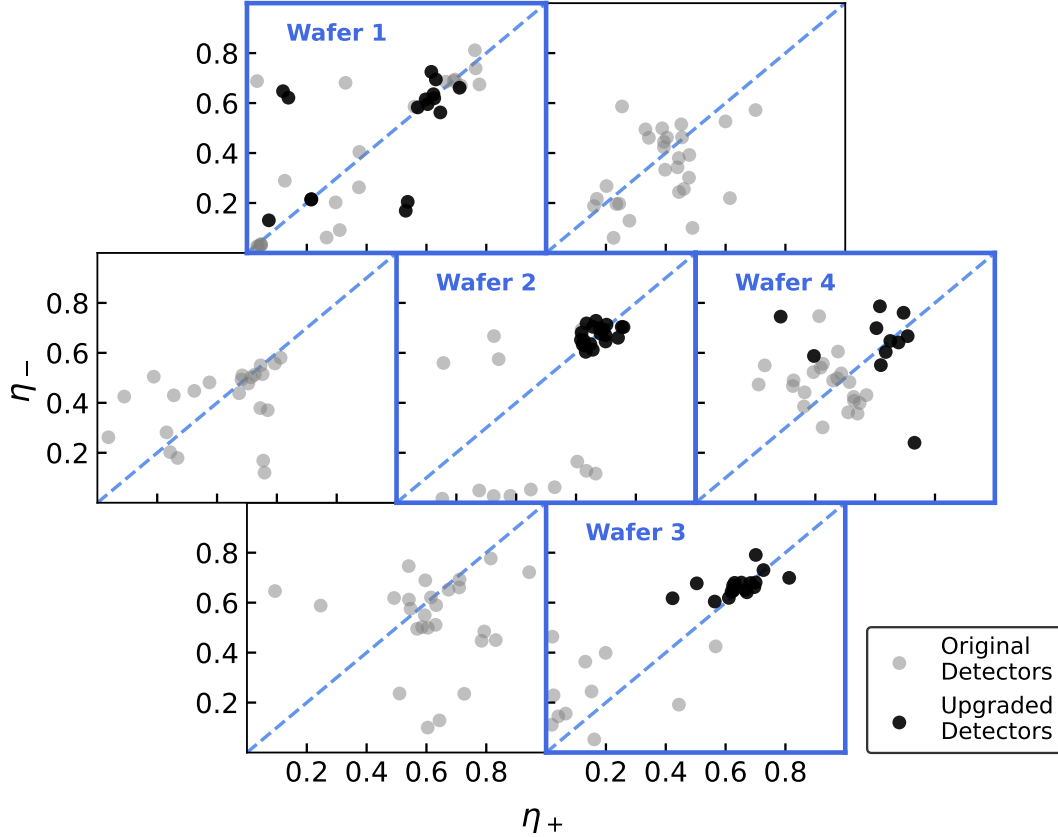


Figure 8. Optical efficiency comparison between paired detectors within a pixel for the original and upgraded focal planes. The optical efficiencies for the $+45^\circ$ and -45° detectors, as labeled in Fig. 1c, are denoted η_+ and η_- . Each subplot represents a wafer on the focal plane. The subplots with blue edges correspond to the four upgraded wafers of the fielded focal plane shown in Figure 1a. The originally fielded detectors are shown in gray, and the upgraded detectors are shown in black. In addition to higher efficiencies, the upgraded detectors have less scatter of relative efficiencies within a detector pair. Fabrication issues with Wafer 1 resulted in a higher number of lower-efficiency detectors; however, these fabrication issues were improved for Wafers 2–4.

Section 3. We differenced the TODs for each polarization pair within a pixel to reduce any correlated noise. The per-detector NEP was then computed by averaging the PSD in the side-bands of the 10 Hz modulation frequency (between 8.0–9.0 Hz and 11.0–12.0 Hz) and dividing by $\sqrt{2}$ (in units of power) to renormalize the pair-differenced noise amplitude to that of a single detector. The final NEP results are robust across a wide range of NEP variance cut thresholds (Section 3). A summary of all NEP estimates is given in Table 3. In this table, we also give the corresponding values for the original CLASS 90 GHz detectors as reported in D22.

Figure 9 shows the measured dark and on-sky NEP compared to the model in Equation 8. For the model, we used the central frequency ν_0 of a diffuse Rayleigh-Jeans source, which approximates the primary sources of loading (atmosphere and optics), and the simulated FWHM bandwidth $\Delta\nu$ reported in Table 2. We also fixed the model at $P_\gamma = 0$ to the dark NEP value. The optical loading P_γ is estimated as the difference between

P_{sat} , measured in laboratory dark tests, and P_J from IV curves at the detector bias point (typically corresponding to $R_{\text{TES}} = 30\%R_N$). As discussed in Appel et al. (2019) (Section 2.1), the saturation power of dark detectors—those bolometers in the array not connected to OMT antennas—drops during sky observations compared to lab measurements taken with the array inside a 1 Kelvin can. We assume this P_{sat} offset impacts both dark and optical detectors equally, leading to an overestimation of on-sky P_γ for optical detectors. To account for this, we introduce another parameter P_{offset} and fit the model (Equation 8) shifted with the substitution $P_\gamma \rightarrow P_\gamma - P_{\text{offset}}$. We found that $P_{\text{offset}} = 1.1$ pW gives a good fit to the data for both the original and upgraded detectors. As in Appel et al. (2019), we hypothesize that the offset is due to optical heating of the detector wafer temperature (and thus increase T_{bath} in Equation 1) above that measured by the focal-plane thermometers. Besides P_{offset} , there are no tunable parameters to the model, which can be seen to fit the data in Figure 9 reasonably well.

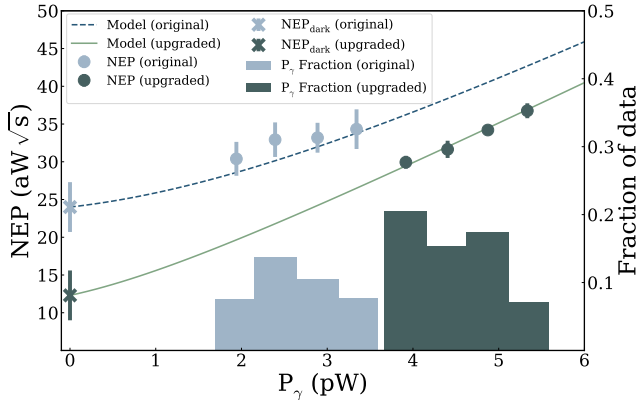


Figure 9. Detector NEP versus optical loading. The dark green (light blue) data points and left axis give the measured NEP as a function of loading for the updated (original) detectors. The original detectors comprise only the three best modules saved for the upgraded array (Figure 1a). Similarly-colored histograms and the right axis show the fraction of data, binned in P_γ , contributing to each data point. Fit to these data, the solid green (blue dashed) line shows the model NEP given in Equation 8 for the updated (original) detectors fit to these data. The black data point at $P_\gamma = 0$ is NEP_{dark} of the updated detectors from in-lab measurements. Despite having a higher P_γ , the new detectors have similar NEP to the originals due to their lower NEP_{dark} .

The data for “Original” wafers included in Figure 9 are from the best three wafers from the original array, which were retained in the upgraded version. (This is why the NEP of the original detectors of $\sim 33 \text{ aW}\sqrt{\text{s}}$ in Figure 9 is significantly lower than the average of $47 \text{ aW}\sqrt{\text{s}}$ quoted for the full original array in Table 3.)

As discussed in Section 6, the upgraded detectors have, on average, higher optical efficiency compared to the originals. This is why, despite the two sets of detectors having similar external (e.g., atmospheric) loading, the upgraded detectors receive a higher optical load in Figure 9. From Equation 8, one would expect the higher P_γ of the upgraded wafers to result in a higher NEP. However, we see in Figure 9 that the NEP is similar between the upgraded detectors and the originals. This is due to the significantly lower NEP_{dark} of the upgraded detectors. This is partially explained by the lower thermal conductivity of the upgraded detectors. Additionally, the original detectors exhibited significant excess noise (Ullom et al. (2004)) above the expected phonon noise level. This excess noise is present in the upgraded detectors but at a much lower level. We conjecture that excess noise in the original detectors stems from internal thermal fluctuations between the TES bilayer and the Pd (de Wit et al. (2021)). In the original TES design the MoAu bilayer is connected to the Pd through long superconducting

Nb leads which establish a weak thermal link. In the upgraded design, MoAu is linked directly to Pd via a normal metal contact, creating a robust thermal connection that minimizes internal thermal fluctuation noise. This internal thermal noise peaks at kHz frequencies, and is aliased down to the signal band due to the limited bandwidth of the time domain multiplexing scheme of the MCE readout.

With the average NEP for the upgraded wafers taken over the dataset shown in Figure 9, we estimated the noise equivalent temperature (NET) for the i^{th} detector, using $\text{NET}_i \approx \text{NEP}_{\text{avg}} \left(\frac{dT_{\text{CMB}}}{dP_\gamma} \right)_i$. The calibration factor between optical power deposited on the bolometer to CMB thermodynamic temperature is given by

$$\frac{dT_{\text{CMB}}}{dP_\gamma} = \frac{dT_{\text{CMB}}}{dT_{\text{RJ}}} \frac{dT_{\text{RJ}}}{dP_\gamma}, \quad (9)$$

where calibration from Rayleigh–Jeans (antenna) temperature to CMB temperature is

$$\frac{dT_{\text{CMB}}}{dT_{\text{RJ}}} = \frac{(e^{x_0} - 1)^2}{x_0^2 e^{x_0}}, \quad (10)$$

with $x_0 = h\nu_0/k_B T_{\text{CMB}}$, and the conversion from optical power to Rayleigh–Jeans temperature is

$$\frac{dT_{\text{RJ}}}{dP_\gamma} = \frac{1}{\eta_i k_B \Delta\nu}, \quad (11)$$

with η_i being the per-detector absolute efficiency from Section 6 and $\Delta\nu$ being the simulated FWHP bandwidth from Table 2. In Table 3, we give the median detector NET and 68% confidence region for each module. We inverse-variance weight the per-detector NETs along with those computed for the original detectors as described in D22 to obtain $\text{NET}_{\text{array}} = 9.7 \mu\text{K}\sqrt{\text{s}}$ for the new array. This is a significant improvement over the original CLASS 90 GHz array, which had an array NET of $19 \mu\text{K}\sqrt{\text{s}}$ (D22).

8. BIAS AND STABILITY IMPROVEMENTS

Each CLASS 90 GHz detector module accepts a single bias-current line from the MCE. The single bias-current runs through an array of identical shunt resistors to provide a single-valued voltage bias (V_{TES}) to all TESs on the detector wafer. We choose V_{TES} to maximize the number of detectors operating at stable points on their superconducting transitions. Conversely, detector wafers with TESs with wide and overlapping voltage bias ranges best accommodate the single V_{TES} value. By satisfying these conditions, the upgraded detectors improve the overall bias-ability of the 90 GHz focal plane.

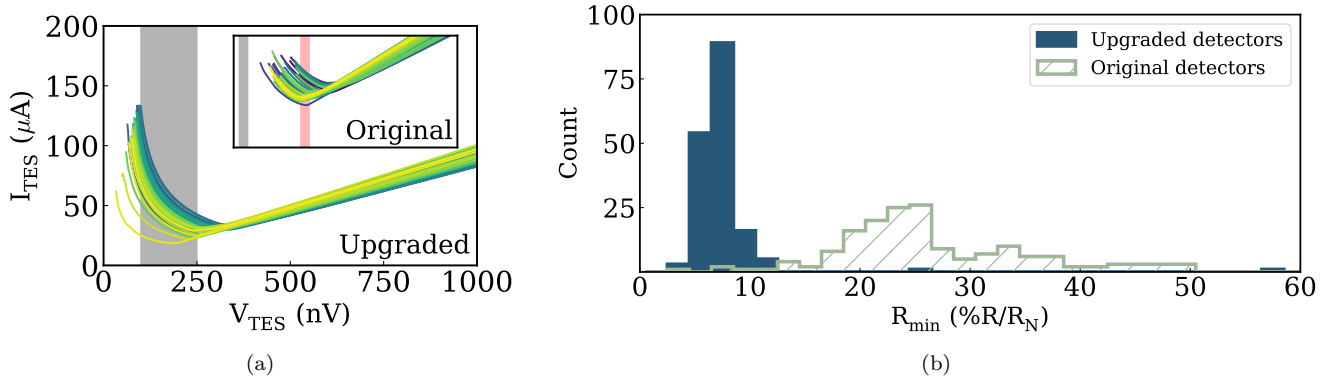


Figure 10. I - V curves (a) for the upgraded detectors on module 2 show a broad range of bias voltages (shaded region 100–250 nV) for which nearly all detectors are on the hyperbola-shaped superconducting transition region. The coloring of the curves is only for visual discrimination; it does not correspond to any physical quantity. The inset plot I - V curves from the original detectors on module W33 require a higher bias target (red shaded region). To maintain all detectors biased above the unstable superconducting I - V endpoint, a larger proportion of the original detectors must operate near their normal resistance, leading to a reduction in the overall array sensitivity. Figure (b) shows the minimum percent R_{N} below which the detectors become unlocked, in an unstable superconducting state. We find that 94% of upgraded detectors are stable down to 15% of their normal resistance. The upgraded detectors allow for a much lower minimum percent R_{N} , increasing the stability of the detectors and widening the biasing window.

The left side of Figure 10 shows a family of I - V curves from detectors on a single wafer (wafer 2). The data were measured in lab during dark testing at a bath temperature of 75 mK. To set the bias, V_{TES} is driven high to force all detectors into their normal state (linear region of the I - V). It is then swept down in steps, bringing the detector from the normal state onto its superconducting transition (hyperbolic region of the I - V). The final value of V_{TES} is chosen to maximize the number of TESs biased near the centers of their transitions. As seen in the figure, there is an ample range in V_{TES} (100–250 nV) for which nearly all detectors are on their transitions.

A useful measure of the quality and width of a detector’s superconducting transition is the minimum resistance R_{min} , expressed as a fraction of R_{N} , below which a TES falls into the superconducting state. This is also a measure of the “stability” of the TES against the onset of electro-thermal runaway at low resistance. The right side of Figure 10 shows that R_{min} for the upgraded detectors is uniformly low with 94% of detectors reaching $R_{\text{min}} < 0.15R_{\text{N}}$. In contrast, the original detectors exhibit a much larger spread and over higher values of R_{min} . A possible reason for the improvement in stability of the upgraded detectors is the addition of a metallic connection between the MoAu superconducting element and the Pd metallization that holds most of the bolometer’s heat capacity.

Finally, while the data in Figure 10 are based on dark tests, during observations the TES bias is set while the detector experiences an optical load. This load moves the transition region of the I - V curve to lower values. The

loading is due primarily to the CMB, the atmosphere, and the optics, which are mostly common to all detectors in a module. Therefore, in principle, optical loading should change the ideal bias voltage in the same way for all detectors, and detectors that shared a common bias in the dark will share a common bias, albeit a different bias, during observations. In practice, however, if the optical efficiencies of the detectors vary too much within a module, the fraction of the loading absorbed will be different for different detectors, creating a variance in the range of acceptable V_{TES} among detectors in the same module. Therefore, the improvement in the uniformity of optical efficiencies achieved with the upgraded design (Figures 7 and 8) also helps us to maximize the number of simultaneously biased detectors and thus improves effective detector yield.

9. CONCLUSIONS

In this paper, we have reported on the performance of upgraded detectors for the CLASS 90 GHz observing band. Four out of seven wafers in the 90 GHz detector array were replaced with upgraded versions. Minor changes to the sensor implementation were motivated by lessons learned modeling the 150/220 detector array. For example, the strategy used for termination of the planar OMTs magic tee and via-less crossovers was revised. These terminations now use a multi-section sub-wavelength absorptive transformer, which is tolerant to metal properties, proximity effect due to superconducting to normal metal contacts, and fabrication misalignment. The most significant design change was at the TES detector, which now benefits from the same lossy transformer

approach for the microwave signal absorption, a reduction in effective enclosure volume, and bias choke filters with higher out-of-band rejection. These electromagnetic and detector electro-thermal circuit modifications (e.g., using a contiguous lumped Pd element on the TES membrane to define the detector speed and stability) have significantly improved the observed performance in the deployed detector arrays. Observations of Jupiter confirm that the telescope optical efficiencies are nearly all above 60%, implying detector efficiencies in excess of 90%. The detector I - V bias curves show that the TESs on a wafer have a broad range of common bias voltages, with 94% of detectors stable down to 15% of the normal resistance. A remaining issue with the detectors is yield in the range of 60%, which we hypothesize is due to defects on the TES bias leads between each device and the bond pads at the edge of the wafer. Yield can be improved by reducing the length of bias leads (e.g., by routing to multiple edges of the wafer) and by removing design elements and steps that produce defects. In particular, routing the leads to two or four sides of the wafer instead of just one would reduce lead length and densities by one-half to one-fourth, significantly lowering the chances for short or open circuits. This is a straightforward way to increase detector yield for a new CLASS detector module or for future applications of these detectors.

We also report detector bandpass and TES electrothermal parameter measurements that match design values except for a lower-than-expected saturation power. Our measurements suggest that this discrepancy would be explained by the thermal conductance prefactor κ being lower than expected. However, we found two alternative scenarios in which κ matches expectations: the median T_c may be 10 mK higher than measured or the power-law index for heat conduction may be $n = 3.77$ instead of the ideal $n = 4$ for ballistic phonon transport. The reality is likely some combination of deviations in T_c , κ , and n from our baseline scenario. Regardless of these as-

sumptions, the resulting lower detector saturation power together with higher optical efficiency results in detectors with significantly lower noise, reducing the array NET from $19 \mu\text{K}\sqrt{\text{s}}$ to $9.7 \mu\text{K}\sqrt{\text{s}}$. The array sensitivity can be further improved by replacing the remaining three original detector wafers with upgraded versions.

ACKNOWLEDGMENTS

We acknowledge the National Science Foundation Division of Astronomical Sciences for their support of CLASS under Grant Numbers 0959349, 1429236, 1636634, 1654494, 2034400, and 2109311. We thank Johns Hopkins University President R. Daniels and the Krieger School of Arts and Sciences Deans for their steadfast support of CLASS. We further acknowledge the very generous support of Jim Murren and Heather Miller (JHU A&S '88), Matthew Polk (JHU A&S Physics BS '71), David Nicholson, and Michael Bloomberg (JHU Engineering '64). The CLASS project employs detector technology developed in collaboration between JHU and Goddard Space Flight Center under several NASA grants. Detector development work at JHU was funded by NASA cooperative agreement 80NSSC19M0005. We acknowledge scientific and engineering contributions from Max Abitbol, Fletcher Boone, David Carcamo, Lance Corbett, Ted Grunberg, Saianeesh Haridas, Jake Hassan, Connor Henley, Ben Keller, Lindsay Lowry, Nick Mehrle, Sasha Novak, Diva Parekh, Isu Ravi, Gary Rhodes, Daniel Swartz, Bingjie Wang, Qinan Wang, Tiffany Wei, Zíang Yan, and Zhuo Zhang. We thank Miguel Angel Díaz, Joseph Zolenas, Jill Hanson, William Deysher, and Chantal Boisvert for logistical support. We acknowledge productive collaboration with the JHU Physical Sciences Machine Shop team. CLASS is located in the Parque Astronómico Atacama in northern Chile under the auspices of the Agencia Nacional de Investigación y Desarrollo (ANID).

APPENDIX

A. DETECTOR PROPERTY SPATIAL VARIATION

Figure 11 shows the distribution of electrothermal properties (T_c , κ , and P_{sat}) and telescope optical efficiency (η) across each of the upgraded wafers. For each pixel on the wafer, the value for each $+45^\circ$ (-45°) detector is shown in the top left (bottom right) of the associated circle. For the most part, the properties are similar between pairs of detectors, and the properties from pixel to pixel vary in a continuous manner (generally linearly) across a wafer. This is what one expects from monotonic variations across the wafer in terms of film depositions, photolithography, and temperature gradients. Wafer 1 shows more spatially random variations than the other wafers. This is likely due to problems encountered during fabrication such that Wafer 1 was designated as “B grade”.

The trends in the electrothermal parameters have expected correlations. For instance, because $P_{\text{sat}} \approx \kappa T_c^n$ we see that the saturation power increases in the same pattern and with non-linear scaling compared to critical temperature. As plotted in Figure 11, the wiring is brought out to bond pads at the bottom of each hexagon of pixels. No trends in the spatial variation of parameters appear to be associated with this symmetry-breaking feature. For the “A grade” Wafers 2, 3, and 4, the telescope optical efficiency is nearly uniform across the wafer and even from wafer to wafer. This indicates that the microwave circuit design is robust to modest fabrication variations that impact the TES electrothermal parameters. Because the optical efficiency includes the effects of the whole telescope, the uniformity of the efficiency also indicates that the optical performance (e.g., beam spill) of the telescope is uniform across the focal plane.

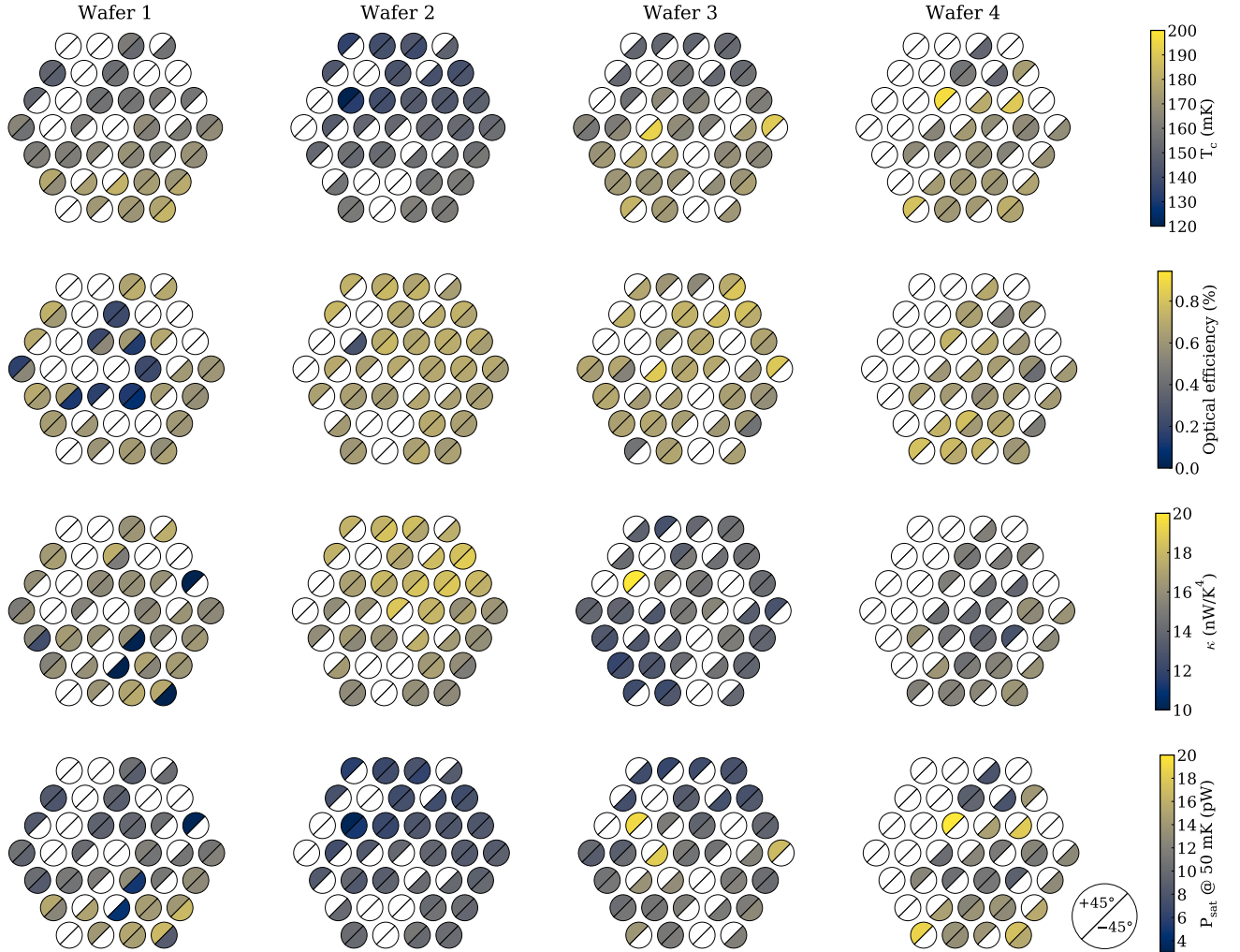


Figure 11. The mapping of several electrothermal parameters from Table 1 and optical efficiency onto the 37 pixels of each upgraded wafer. Each pixel contains two detectors, corresponding to $+45^\circ$ (top left of corresponding circles) and -45° (bottom right of corresponding circles) as shown in Figure 1c. No color indicates an absence of a working detector. Low detector yield is likely due to opens and shorts along the bias leads extending from the detector pixels to the bondpads at the edge of the wafer.

B. PARAMETER QUICK REFERENCE

REFERENCES

- Addamo, G., Ade, P. A. R., Baccigalupi, C., et al. 2021, JCAP, 2021, 008, doi: [10.1088/1475-7516/2021/08/008](https://doi.org/10.1088/1475-7516/2021/08/008)
- Ali, A. M., Essinger-Hileman, T., Marriage, T., et al. 2022, Review of Scientific Instruments, 93, 024503, doi: [10.1063/5.0049526](https://doi.org/10.1063/5.0049526)

The detector parameters defined in the main text are referenced in Table 4, along with their estimation method, equations, and an index of sections where each appears.

Table 4. Quick Reference and Section Index for Parameters

Name	Symbol	Estimation Method and Equations	Sections ^a
Bias (Joule) Power	P_J	Measured $P_J = I_{\text{TES}} \times V_{\text{TES}}$	4.1*, 4.3
Saturation Power	P_{sat}	$P_{\text{sat}} = P_J$ for $P_\gamma = 0$ and $R_{\text{TES}} = 0.7R_N$	4.1*
Photon Power	P_γ	$P_\gamma = P_{\text{sat}} - P_J$	4.3*, 7
Critical Temperature	T_c	$P_{\text{sat}} = \kappa (T_c^n - T_{\text{bath}}^n)$ fit to IV Data	2.2, 4.2*, 4.4, 7
Bath Temperature	T_{bath}	Measured by Thermometry	2.2, 4.2, 7
Normal Resistance	R_N	$I_{\text{TES}} = V_{\text{TES}}/R_N$ fit to normal- <i>TES</i> IV data	4.1*
Thermal Conductance Prefactor	κ	$P_{\text{sat}} = \kappa (T_c^n - T_{\text{bath}}^n)$ fit to IV Data	4.2*, 4.4
Thermal Conductance Index	n	$n = 4$ for ballistic phonons	4.2, 4.4
Thermal Conductance ^b	G	$G = n\kappa T_c^{n-1} \approx nP_{\text{sat}}/T_c$	4.2*
Heat Capacity	C	$C = G\tau$	2.2, 4.3*, 4.4
Thermal Time Constant	τ	(Appel et al. 2022, Eq. 26) given τ_γ	4.3*
Optical Time Constant	τ_γ	Measured from VPM Emission	4.3*
Bandwidth	$\Delta\nu$	Simulation checked with FTS measurement	5*
Bandcenter	ν_0	Simulation checked with FTS measurement	5*
Telescope Optical Efficiency	η	Measured with Planet Observations	6*
Phonon NEP	$\text{NEP}_{\text{phonon}}$	$\text{NEP}_{\text{phonon}} = (2k_B T_c^2 G F_{\text{link}})^{1/2}$	7
	F_{link}	$F_{\text{link,phonon}} = (1 + (T_{\text{bath}}/T_c)^{n+1})/2 \approx 1/2$	7
Dark NEP ^c	NEP_{dark}	Measured in Dark Configuration	7*
Photon NEP	NEP_γ	$(\text{NEP}_\gamma)^2 = h\nu_0 P_\gamma + P_\gamma^2/\Delta\nu$	7*
Total NEP	NEP	Measured from Survey Data $(\text{NEP})^2 = (\text{NEP}_\gamma)^2 + (\text{NEP}_{\text{dark}})^2$	7*

^aSections with a star denote where measurements are described. Otherwise section designation indicates parts of the text in which the parameter is described or plays a role in the discussion.

^bThe approximation given for this parameter assumes $T_c^n \gg T_{\text{bath}}^n$, which is valid for CLASS.

^cDark NEP includes the Phonon NEP as well as any other contributions to total NEP (e.g., from the SQUID readout or excess noise due to a non-trivial TES thermal circuit) besides the photon NEP.

- Appel, J. W., Ali, A., Amiri, M., et al. 2014, in Society of Photo-Optical Instrumentation Engineers (SPIE) Conference Series, Vol. 9153, Millimeter, Submillimeter, and Far-Infrared Detectors and Instrumentation for Astronomy VII, 91531J, doi: [10.1117/12.2056530](https://doi.org/10.1117/12.2056530)
- Appel, J. W., Xu, Z., Padilla, I. L., et al. 2019, *ApJ*, 876, 126, doi: [10.3847/1538-4357/ab1652](https://doi.org/10.3847/1538-4357/ab1652)
- Appel, J. W., Bennett, C. L., Brewer, M. K., et al. 2022, *ApJS*, 262, 52, doi: [10.3847/1538-4365/ac8cf2](https://doi.org/10.3847/1538-4365/ac8cf2)
- Arnold, K., Ade, P. A. R., Anthony, A. E., et al. 2012, in Society of Photo-Optical Instrumentation Engineers (SPIE) Conference Series, Vol. 8452, Millimeter, Submillimeter, and Far-Infrared Detectors and Instrumentation for Astronomy VI, ed. W. S. Holland & J. Zmuidzinas, 84521D, doi: [10.1117/12.927057](https://doi.org/10.1117/12.927057)
- Battistelli, E. S., Amiri, M., Burger, B., et al. 2008, *Journal of Low Temperature Physics*, 151, 908, doi: [10.1007/s10909-008-9772-z](https://doi.org/10.1007/s10909-008-9772-z)
- Bennett, C. L., Larson, D., Weiland, J. L., et al. 2013, *ApJS*, 208, 20, doi: [10.1088/0067-0049/208/2/20](https://doi.org/10.1088/0067-0049/208/2/20)
- BICEP/Keck Collaboration, Ade, P. A. R., Ahmed, Z., et al. 2021, *PhRvL*, 127, 151301, doi: [10.1103/PhysRevLett.127.151301](https://doi.org/10.1103/PhysRevLett.127.151301)
- Boyle, W. S., & Rodgers, K. F., J. 1959, *Journal of the Optical Society of America* (1917-1983), 49, 66
- Chuss, D. T., Ali, A., Amiri, M., et al. 2016, *Journal of Low Temperature Physics*, 184, 759, doi: [10.1007/s10909-015-1368-9](https://doi.org/10.1007/s10909-015-1368-9)
- Cleary, J. 2023, PhD thesis, Johns Hopkins University
- CMB-S4 Collaboration, Abazajian, K., Addison, G. E., et al. 2022, *ApJ*, 926, 54, doi: [10.3847/1538-4357/ac1596](https://doi.org/10.3847/1538-4357/ac1596)
- Crowe, E. J., Bennett, C. L., Chuss, D. T., et al. 2013, *IEEE Transactions on Applied Superconductivity*, 23, 2500505, doi: [10.1109/TASC.2012.2237211](https://doi.org/10.1109/TASC.2012.2237211)
- Dahal, S., Ali, A., Appel, J. W., et al. 2018, in Society of Photo-Optical Instrumentation Engineers (SPIE) Conference Series, Vol. 10708, Society of Photo-Optical Instrumentation Engineers (SPIE) Conference Series, 107081Y, doi: [10.1117/12.2311812](https://doi.org/10.1117/12.2311812)
- Dahal, S., Amiri, M., Appel, J. W., et al. 2020, *Journal of Low Temperature Physics*, 199, 289, doi: [10.1007/s10909-019-02317-0](https://doi.org/10.1007/s10909-019-02317-0)
- Dahal, S., Appel, J. W., Datta, R., et al. 2022, *ApJ*, 926, 33, doi: [10.3847/1538-4357/ac397c](https://doi.org/10.3847/1538-4357/ac397c)
- Datta, R., Brewer, M. K., Couto, J. D., et al. 2024, *ApJS*, 273, 26, doi: [10.3847/1538-4365/ad50a0](https://doi.org/10.3847/1538-4365/ad50a0)
- de Wit, M., Gottardi, L., Taralli, E., et al. 2021, *Physical Review Applied*, 16, 044059, doi: [10.1103/PhysRevApplied.16.044059](https://doi.org/10.1103/PhysRevApplied.16.044059)
- Denis, K. L., Cao, N. T., Chuss, D. T., et al. 2009, in American Institute of Physics Conference Series, Vol. 1185, The Thirteenth International Workshop on Low Temperature Detectors - LTD13, ed. B. Young, B. Cabrera, & A. Miller, 371–374, doi: [10.1063/1.3292355](https://doi.org/10.1063/1.3292355)
- Dorise, W. B., Morgan, K. M., Bennett, D. A., et al. 2016, *Journal of Low Temperature Physics*, 184, 389, doi: [10.1007/s10909-015-1373-z](https://doi.org/10.1007/s10909-015-1373-z)
- Eimer, J. R., Bennett, C. L., Chuss, D. T., et al. 2012, in Society of Photo-Optical Instrumentation Engineers (SPIE) Conference Series, Vol. 8452, Millimeter, Submillimeter, and Far-Infrared Detectors and Instrumentation for Astronomy VI, ed. W. S. Holland & J. Zmuidzinas, 845220, doi: [10.1117/12.925464](https://doi.org/10.1117/12.925464)
- Essinger-Hileman, T., Ali, A., Amiri, M., et al. 2014, in Society of Photo-Optical Instrumentation Engineers (SPIE) Conference Series, Vol. 9153, Millimeter, Submillimeter, and Far-Infrared Detectors and Instrumentation for Astronomy VII, ed. W. S. Holland & J. Zmuidzinas, 91531I, doi: [10.1117/12.2056701](https://doi.org/10.1117/12.2056701)
- Harrington, K., Marriage, T., Ali, A., et al. 2016, in Society of Photo-Optical Instrumentation Engineers (SPIE) Conference Series, Vol. 9914, Millimeter, Submillimeter, and Far-Infrared Detectors and Instrumentation for Astronomy VIII, ed. W. S. Holland & J. Zmuidzinas, 99141K, doi: [10.1117/12.2233125](https://doi.org/10.1117/12.2233125)
- Harrington, K., Eimer, J., Chuss, D. T., et al. 2018, in Society of Photo-Optical Instrumentation Engineers (SPIE) Conference Series, Vol. 10708, Society of Photo-Optical Instrumentation Engineers (SPIE) Conference Series, 107082M, doi: [10.1117/12.2313614](https://doi.org/10.1117/12.2313614)
- Hinshaw, G., Larson, D., Komatsu, E., et al. 2013, *ApJS*, 208, 19, doi: [10.1088/0067-0049/208/2/19](https://doi.org/10.1088/0067-0049/208/2/19)
- Hui, H., Ade, P. A. R., Ahmed, Z., et al. 2016, in Society of Photo-Optical Instrumentation Engineers (SPIE) Conference Series, Vol. 9914, Millimeter, Submillimeter, and Far-Infrared Detectors and Instrumentation for Astronomy VIII, ed. W. S. Holland & J. Zmuidzinas, 99140T, doi: [10.1117/12.2232986](https://doi.org/10.1117/12.2232986)
- Irwin, K. D., & Hilton, G. C. 2005, in *Cryogenic Particle Detection*, ed. C. Enss, Vol. 99, 63, doi: [10.1007/10933596_3](https://doi.org/10.1007/10933596_3)
- Iuliano, J. 2020, PhD thesis, Johns Hopkins University
- Iuliano, J., Eimer, J., Parker, L., et al. 2018, in Society of Photo-Optical Instrumentation Engineers (SPIE) Conference Series, Vol. 10708, Society of Photo-Optical Instrumentation Engineers (SPIE) Conference Series, 1070828, doi: [10.1117/12.2312954](https://doi.org/10.1117/12.2312954)
- Kittel, C. 1996, *Introduction to Solid State Physics*, 7th edn. (New York: John Wiley & Sons)

- Kuo, C. L., Bock, J. J., Bonetti, J. A., et al. 2008, in Society of Photo-Optical Instrumentation Engineers (SPIE) Conference Series, Vol. 7020, Millimeter and Submillimeter Detectors and Instrumentation for Astronomy IV, ed. W. D. Duncan, W. S. Holland, S. Withington, & J. Zmuidzinas, 70201I, doi: [10.1117/12.788588](https://doi.org/10.1117/12.788588)
- Lazear, J., Ade, P. A. R., Benford, D., et al. 2014, in Society of Photo-Optical Instrumentation Engineers (SPIE) Conference Series, Vol. 9153, Millimeter, Submillimeter, and Far-Infrared Detectors and Instrumentation for Astronomy VII, ed. W. S. Holland & J. Zmuidzinas, 91531L, doi: [10.1117/12.2056806](https://doi.org/10.1117/12.2056806)
- Lee, K., Choi, J., Génova-Santos, R. T., et al. 2020, Journal of Low Temperature Physics, 200, 384, doi: [10.1007/s10909-020-02511-5](https://doi.org/10.1007/s10909-020-02511-5)
- LiteBIRD Collaboration, Allys, E., Arnold, K., et al. 2022, arXiv e-prints, arXiv:2202.02773, doi: [10.48550/arXiv.2202.02773](https://doi.org/10.48550/arXiv.2202.02773)
- May, J. L., Adler, A. E., Ausermann, J. E., et al. 2024, in Ground-based and Airborne Telescopes X, ed. H. K. Marshall, J. Spyromilio, & T. Usuda, Vol. 13094, International Society for Optics and Photonics (SPIE), 1309432, doi: [10.1117/12.3019051](https://doi.org/10.1117/12.3019051)
- Morgan, M. A., & Pan, S.-K. 2013, IEEE Transactions on Terahertz Science and Technology, 3, 72, doi: [10.1109/TTHZ.2012.2235910](https://doi.org/10.1109/TTHZ.2012.2235910)
- Nagler, P. C., Sadleir, J. E., & Wollack, E. J. 2020, arXiv e-prints, arXiv:2012.06543, <https://arxiv.org/abs/2012.06543>
- Niemack, M. D., Zhao, Y., Wollack, E., et al. 2008, Journal of Low Temperature Physics, 151, 690, doi: [10.1007/s10909-008-9729-2](https://doi.org/10.1007/s10909-008-9729-2)
- Núñez, C., Appel, J. W., Bruno, S. M., et al. 2022, in Society of Photo-Optical Instrumentation Engineers (SPIE) Conference Series, Vol. 12190, Millimeter, Submillimeter, and Far-Infrared Detectors and Instrumentation for Astronomy XI, ed. J. Zmuidzinas & J.-R. Gao, 121901J, doi: [10.1117/12.2630081](https://doi.org/10.1117/12.2630081)
- Núñez, C., Appel, J. W., Brewer, M. K., et al. 2023, IEEE Transactions on Applied Superconductivity, 33, 3262497, doi: [10.1109/TASC.2023.3262497](https://doi.org/10.1109/TASC.2023.3262497)
- Pan, Z., Liu, M., Basu Thakur, R., et al. 2019, ApOpt, 58, 6257, doi: [10.1364/AO.58.006257](https://doi.org/10.1364/AO.58.006257)
- Planck Collaboration, Ade, P. A. R., Aghanim, N., et al. 2016, A&A, 594, A5, doi: [10.1051/0004-6361/201526632](https://doi.org/10.1051/0004-6361/201526632)
- Planck Collaboration, Aghanim, N., Akrami, Y., et al. 2020, A&A, 641, A6, doi: [10.1051/0004-6361/201833910](https://doi.org/10.1051/0004-6361/201833910)
- Posada, C. M., Ade, P. A. R., Anderson, A. J., et al. 2016, in Society of Photo-Optical Instrumentation Engineers (SPIE) Conference Series, Vol. 9914, Millimeter, Submillimeter, and Far-Infrared Detectors and Instrumentation for Astronomy VIII, ed. W. S. Holland & J. Zmuidzinas, 991417, doi: [10.1117/12.2232912](https://doi.org/10.1117/12.2232912)
- Reintsema, C. D., Beyer, J., Nam, S. W., et al. 2003, Review of Scientific Instruments, 74, 4500, doi: [10.1063/1.1605259](https://doi.org/10.1063/1.1605259)
- Rostem, K., Bennett, C. L., Chuss, D. T., et al. 2012, in Society of Photo-Optical Instrumentation Engineers (SPIE) Conference Series, Vol. 8452, Millimeter, Submillimeter, and Far-Infrared Detectors and Instrumentation for Astronomy VI, ed. W. S. Holland & J. Zmuidzinas, 84521N, doi: [10.1117/12.927056](https://doi.org/10.1117/12.927056)
- Rostem, K., Chuss, D. T., Colazo, F. A., et al. 2014, Journal of Applied Physics, 115, 124508, doi: [10.1063/1.4869737](https://doi.org/10.1063/1.4869737)
- Rostem, K., Ali, A., Appel, J. W., et al. 2016, in Society of Photo-Optical Instrumentation Engineers (SPIE) Conference Series, Vol. 9914, Millimeter, Submillimeter, and Far-Infrared Detectors and Instrumentation for Astronomy VIII, ed. W. S. Holland & J. Zmuidzinas, 99140D, doi: [10.1117/12.2234308](https://doi.org/10.1117/12.2234308)
- Rubiño-Martín, J. A., Guidi, F., Génova-Santos, R. T., et al. 2023, MNRAS, 519, 3383, doi: [10.1093/mnras/stac3439](https://doi.org/10.1093/mnras/stac3439)
- Sadleir, J. E., Smith, S. J., Bandler, S. R., Chervenak, J. A., & Clem, J. R. 2010, PhRvL, 104, 047003, doi: [10.1103/PhysRevLett.104.047003](https://doi.org/10.1103/PhysRevLett.104.047003)
- Shirokoff, E., Benson, B. A., Bleem, L. E., et al. 2009, IEEE Transactions on Applied Superconductivity, 19, 517, doi: [10.1109/TASC.2009.2018229](https://doi.org/10.1109/TASC.2009.2018229)
- Simons Observatory Collaboration, Ade, P., Aguirre, J., et al. 2019, JCAP, 2019, 056, doi: [10.1088/1475-7516/2019/02/056](https://doi.org/10.1088/1475-7516/2019/02/056)
- Staguhn, J. G., Benford, D. J., Chervenak, J. A., et al. 2004, in Society of Photo-Optical Instrumentation Engineers (SPIE) Conference Series, Vol. 5498, Z-Spec: a broadband millimeter-wave grating spectrometer: design, construction, and first cryogenic measurements, ed. C. M. Bradford, P. A. R. Ade, J. E. Aguirre, J. J. Bock, M. Dragovan, L. Duband, L. Earle, J. Glenn, H. Matsuhara, B. J. Naylor, H. T. Nguyen, M. Yun, & J. Zmuidzinas, 390–395, doi: [10.1117/12.552102](https://doi.org/10.1117/12.552102)
- Suzuki, A., Arnold, K., Edwards, J., et al. 2012, Journal of Low Temperature Physics, 167, 852, doi: [10.1007/s10909-012-0602-y](https://doi.org/10.1007/s10909-012-0602-y)
- U-yen, K., & Wollack, E. J. 2008, in 2008 38th European Microwave Conference, 642–645, doi: [10.1109/EUMC.2008.4751534](https://doi.org/10.1109/EUMC.2008.4751534)

- U-yen, K., Wollack, E. J., Moseley, S. H., et al. 2009, in 2009 IEEE MTT-S International Microwave Symposium Digest, 1029–1032, doi: [10.1109/MWSYM.2009.5165875](https://doi.org/10.1109/MWSYM.2009.5165875)
- U-Yen, K., Wollack, E. J., Papapolymerou, J., & Laskar, J. 2008, IEEE Transactions on Microwave Theory Techniques, 56, 172, doi: [10.1109/TMTT.2007.912213](https://doi.org/10.1109/TMTT.2007.912213)
- Ullom, J. N., Doriese, W. B., Hilton, G. C., et al. 2004, Applied Physics Letters, 84, 4206, doi: [10.1063/1.1753058](https://doi.org/10.1063/1.1753058)
- Watts, D. J., Larson, D., Marriage, T. A., et al. 2015, ApJ, 814, 103, doi: [10.1088/0004-637X/814/2/103](https://doi.org/10.1088/0004-637X/814/2/103)
- Watts, D. J., Wang, B., Ali, A., et al. 2018, ApJ, 863, 121, doi: [10.3847/1538-4357/aad283](https://doi.org/10.3847/1538-4357/aad283)
- Wei, T. 2012, Bachelor's thesis, Johns Hopkins University, Maryland
- Zeng, L., Bennett, C. L., Chuss, D. T., & Wollack, E. J. 2010, in Society of Photo-Optical Instrumentation Engineers (SPIE) Conference Series, Vol. 7741, Millimeter, Submillimeter, and Far-Infrared Detectors and Instrumentation for Astronomy V, ed. W. S. Holland & J. Zmuidzinas, 774129, doi: [10.1117/12.857679](https://doi.org/10.1117/12.857679)